Flow-Induced Symmetry Breaking in Growing Bacterial Biofilms

Philip Pearce [ORCID],[1] Boya Song,[1] Dominic J. Skinner,[1] Rachel Mok,[1,2] Raimo Hartmann,[3] Praveen K. Singh,[3]
Hannah Jeckel,[3,5] Jeffrey S. Oishi [ORCID],[1,4] Knut Drescher [ORCID],[3,5,*] and Jörn Dunkel [ORCID][1,†]

[1]*Department of Mathematics, Massachusetts Institute of Technology, Cambridge Massachusetts 02139-4307, USA*
[2]*Department of Mechanical Engineering, Massachusetts Institute of Technology, Cambridge, Massachusetts 02139-4307, USA*
[3]*Max Planck Institute for Terrestrial Microbiology, 35043 Marburg, Germany*
[4]*Department of Physics, Bates College, Lewiston, Maine 04240, USA*
[5]*Department of Physics, Philipps-Universität Marburg, 35043 Marburg, Germany*

Bacterial biofilms represent a major form of microbial life on Earth and serve as a model active nematic system, in which activity results from growth of the rod-shaped bacterial cells. In their natural environments, ranging from human organs to industrial pipelines, biofilms have evolved to grow robustly under significant fluid shear. Despite intense practical and theoretical interest, it is unclear how strong fluid flow alters the local and global architectures of biofilms. Here, we combine highly time-resolved single-cell live imaging with 3D multiscale modeling to investigate the mechanisms by which flow affects the dynamics of all individual cells in growing biofilms. Our experiments and cell-based simulations reveal three quantitatively different growth phases in strong external flow and the transitions between them. In the initial stages of biofilm development, flow induces a downstream gradient in cell orientation, causing asymmetrical dropletlike biofilm shapes. In the later developmental stages, when the majority of cells are sheltered from the flow by the surrounding extracellular matrix, buckling-induced cell verticalization in the biofilm core restores radially symmetric biofilm growth, in agreement with predictions of a 3D continuum model.

Fluid flow is a key element of many natural and industrial environments in which bacteria form biofilms, from rivers [1], pipes [2], and filtration devices [3] to the human heart [4], intestines [5], and mouth [6]. Owing to their prevalence in such environments, biofilms cause major economic and health burdens to society. Hydrodynamic effects have been found to play a crucial role during the initial attachment of cells to surfaces [7]. Later in development, flow provides nutrients to surface-attached biofilm communities, while removing metabolic waste products and signaling molecules [8–10]. There is therefore strong practical and theoretical interest in understanding the interaction between biofilms and external flow fields [8,11]. Identifying the multiscale dynamics of such growth-active nematics under the influence of shear will be helpful when adapting current theories for active matter [12,13] to describe and predict bacterial biofilm growth across model systems and species [14,15].

Imposed fluid shear has been observed to produce striking aerofoil-like shapes [16–18] during the early stages of biofilm growth and, in some cases, long filaments or streamers that extend far downstream [1,19]. It has often been assumed that the key driver of the observed architecture of biofilms in flow is bulk deformation or erosion of biofilm biomass [16,19,20]. Recently, new imaging

methodologies were developed to quantify biofilm dynamics at single-cell resolution, yet these studies have focused on conditions with very low flow [17,21–23]. Earlier work that quantified biofilm architecture in high flow did not resolve the microscopic dynamics [1,19] or did not explain the mechanisms by which high shear modifies the microscopic and macroscopic biofilm architecture [17]. Despite the new imaging techniques and the extensive environmental relevance of flow-biofilm interactions, it has therefore remained unclear how flow reorients cells in space and time during biofilm growth and, in turn, how these microscopic cellular reorientations contribute to the overall biofilm morphogenesis.

Here, we investigate comprehensively the effects of high fluid shear on individual cell dynamics within growing *Vibrio cholerae* biofilms, by combining multiscale modeling with highly time-resolved imaging at single-cell resolution (Fig. 1). First, we establish the translational and orientational dynamics of cells within early stage biofilm microcolonies in strong flow, by constraining an individual cell-based model with the imaging data. Subsequently, these dynamics are included in a minimal continuum model that identifies the physical processes necessary to explain the biofilm architectural development observed at the later stages. We find that the bulk biofilm dynamics are determined almost entirely by cellular orientations inside
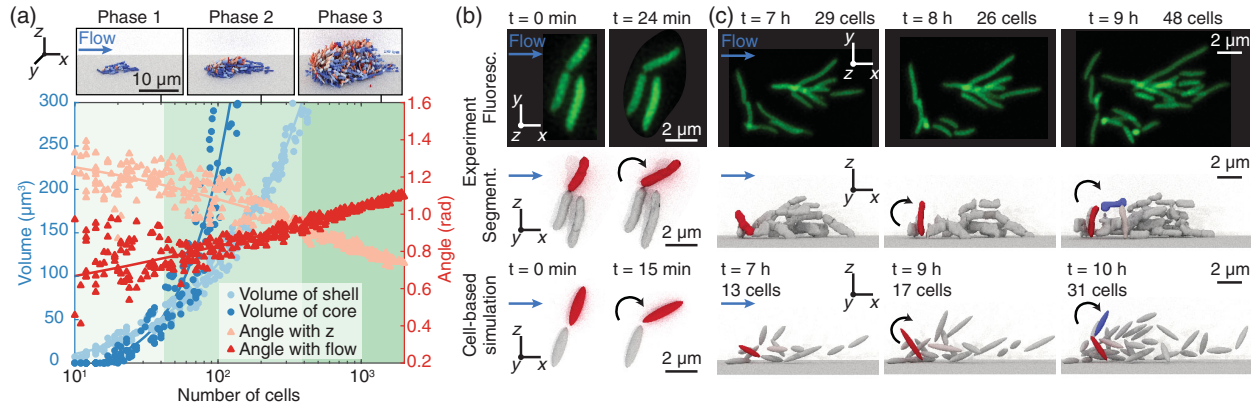
FIG. 1. The three phases of *V. cholerae* biofilm growth and hydrodynamic cell alignment mechanisms in strong flow. (a) The transition from the 2D surface-dominated growth phase 1 (light green) to the 3D bulk-dominated phase 2 (green) occurs when the volume of the biofilm shell (light blue circles) equals the volume of the biofilm core (dark blue circles); see Supplemental Material [27] for details of the volume measurements. The transition to the verticalization phase 3 (dark green) occurs when the average cell-orientation angles with z (light red triangles) and the flow direction (dark red triangles) cross. The diagram shows the combined data from $n = 3$ independent biofilm experiments, with typical snapshots of biofilms in each phase above (Video S1). (b),(c) Flow-induced cell reorientation dynamics in the initial phase of biofilm growth. (b) Cells in direct contact with the surface align with the flow as a result of a torque generated by a combination of the fluid drag and asymmetrical attachment to their parent cell at the pole; see also Fig. S10 for additional intermediate snapshots [27]. Fluorescence images show projection of a confocal z stack. (c) Cells at the front of the biofilm (red) align vertically as a result of the torques τ_{drag} and τ_{shear} (see also Fig. S11). When a vertically oriented cell (red) divides, the daughter cell (blue), if exposed to shear, aligns with the flow.

the biofilm, representing the local flow-induced nematic director field, rather than by biofilm deformation or cell erosion as has been previously hypothesized [8,17].

To investigate the effects of strong flow on biofilms, we imaged biofilm development on glass surfaces at cellular resolution in a flow channel with a shear rate of 2000 s^{-1} (Re $\approx$ 1), which is a typical order of magnitude for flows in natural and man-made environments containing bacteria [24–26]. To achieve the required time resolution, adaptive confocal microscopy was combined with ground-truth-calibrated 3D image segmentation suitable for our model organism: *V. cholerae* with a straight cell shape ($\Delta crvA$), constitutively expressing a green fluorescent protein (sfGFP) [Figs. 1(b) and 1(c); Supplemental Material [27]]. Using a time resolution $\Delta t = 6$ min, we visualized transient cell reorientations caused by the flow [Figs. 1(b) and 1(c)], in addition to reconstructing cell lineages and measuring cellular growth rates. By combining these data with previously obtained data for larger biofilms [17], we obtained a comprehensive dataset showing the effects of strong fluid flow on biofilms growing from a single founder cell up to more than 2000 cells (Video S1 [27]).

To understand the mechanical processes determining the shape and architecture of biofilms in flow, we developed a 3D multiscale theoretical framework consisting of two separate models: a cell-based model (Video S2) and a continuum model (Video S3). Cells are represented as growing, dividing ellipsoids with pairwise interactions, as defined in Ref. [17]; parameters of this model were determined from single-cell biofilm experiments (Table SII in Supplemental Material [27]). Movement of cells occurs

through growth and cellular interactions mediated by extracellular matrix and adhesion proteins, but no active motility exists inside *V. cholerae* biofilms. The cell-based model from Ref. [17] was then extended to include flow, as well as previously neglected physical effects that determine biofilm architecture at the single-cell level in strong-flow environments (Supplemental Material [27]). In particular, each cell feels a force and torque dependent upon its orientation relative to the shear flow; the streamlines of the flow are deformed by the biofilm in a manner consistent with an approximately hemispherical object. Furthermore, the experimental observation that parent and daughter cells adhere to each other at the cell pole for approximately one division time [Fig. 1(b)] was implemented using Hookean springs, which connect the nearest polar end points of these cells and persist for 90% of a division time.

In the complementary continuum model, movement and alignment of biofilm matter is represented through a local mean velocity field $v(t, x)$ and nematic "Q tensor" $Q = S(nn - 1/3)$ [12,13,28], where $S(t, x)$ is the nematic order parameter and $n(t, x)$ is the nematic director field of cellular orientations. Within the biofilm, a modified incompressibility condition $\nabla \cdot v = g$ enforces constant growth with rate g; the assumption of a uniform growth rate g is valid as long as all cells have access to sufficient nutrients, which holds for the experimental conditions considered here (Fig. S4 [27]). The effect of this growth, which is directed nematically because cells elongate and divide along their longest axis [29], is imposed by including an additional active term in the stress [30,31]. Over growth timescales, the passive part of the constitutive relationship

can be approximated as purely viscous with effective viscosity μ, yielding a stress tensor $\boldsymbol{\sigma} = -p\mathbf{1} + \mu(\nabla\boldsymbol{v} + \nabla\boldsymbol{v}^T) - 2\mu g\boldsymbol{Q}$ (Supplemental Material [27]), where p is the pressure. This constitutive law was simulated in the open-source solver DEDALUS [32], using a phase-field variable to track the expansion of the biofilm [33,34]. The nematic order field was imposed such that $\boldsymbol{n}(t,\boldsymbol{x})$ rotates from vertical to an angle just beyond horizontal at the biofilm's back and sides over a specified length. These rotation lengths in each direction were the key parameters in the model and were chosen to give quantitative agreement with measured cell alignment fields (Fig. S6 [27]). The initial biofilm shape was always taken to be spherically symmetric, so that any asymmetry in the shape was induced by growth along the imposed nematic director field. Using this model, we could assess to what extent the observed cell alignment fields determined biofilm growth and shape. The combined multiscale models and experiments revealed that the full growth and cellular alignment program of bacterial biofilms in flow can be categorized into three distinct physical phases [Fig. 1(a)].

During the initial biofilm growth phase [Figs. 1(b) and 1(c)], the majority of cells are exposed to the flow. We found that the presence of strong shear breaks the otherwise hemispherically symmetric colony growth, and two key physical processes dominate the cell alignment dynamics. We describe and illustrate these two key processes using a combination of scaling laws and the cell-based model. First, daughter cells are reoriented after division to align with the flow by a drag-induced torque caused by the combination of the flow and the polar adhesion to their parent cell [Fig. 1(b)]. Specifically, a horizontal ellipsoidal cell of length l and width r constrained at one pole, with its longest axis perpendicular to a flow of speed U, is expected to feel a torque $\tau_{\text{drag}} \sim Dl$, where D is the drag $D \sim G_1\mu lU$; here G_1 is a geometric factor [35]. Thus, using $\boldsymbol{v} = \dot{\gamma}z\hat{\mathbf{x}}$, we have $\tau_{\text{drag}} \sim G_1\mu l^2 h\dot{\gamma}$, where h is the height of the cell centroid from the surface. Second, the shear in the z direction applies a torque, causing a cell's longest axis to rotate about the axis perpendicular to the plane of the flow [36]. For a horizontal cell whose longest axis is parallel to the flow, this torque is approximately $\tau_{\text{shear}} \sim G_2\mu lr^2\dot{\gamma}$; here G_2 is a second geometric factor [37]. Both torques τ_{drag} and τ_{shear} are expected to be of the same order of magnitude $\tau \sim 1 \text{ pN}\,\mu\text{m}$, which is not strong enough to rip fully surface-attached cells from the surface [23]. However, the flow-induced torques act together to cause the verticalization of daughter cells at
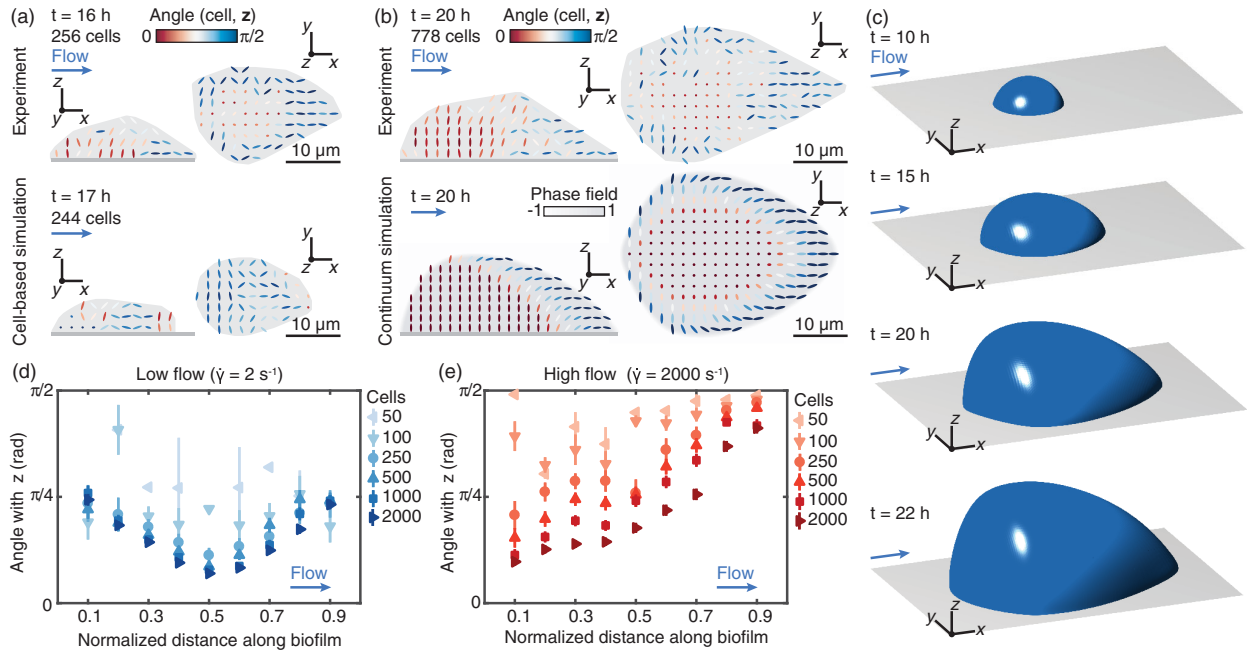

FIG. 2. A wave of cell verticalization travels downstream through the biofilm in the second phase of biofilm growth. (a) At the beginning of this phase, a small group of cells is verticalized at the front of the biofilm by a combination of cell-cell interactions and fluid shear. (b) The fraction of vertical cells increases as the biofilm grows. The downstream region of flow-aligned cells leads to distinctive dropletlike shapes that are captured in (a) cell-based (Video S2) and (b) continuum simulations (Video S3) [27]. For the experiments ($n = 3$) and cell-based simulations ($n = 10$), the gray area denotes the region inside the convex hull around grid points with a cell number density higher than 0.1 μm^{-3} per biofilm. (c) 3D renderings of shapes generated by the continuum simulations. The isosurface $\phi = 0$ of the phase-field variable ϕ is shown (Supplemental Material [27]). (d) In low-flow environments, a central core of the biofilm is verticalized owing to a buckling instability induced by growth and surface attachment. (e) Strong flow causes symmetry breaking and a growing group of vertically aligned cells at the front of the biofilm. Error bars show the standard error for grid points spaced 2 μm throughout $n = 3$ biofilms in each case.

the front of the biofilm that are not fully surface attached [38,39] or that have been partially verticalized by a peeling instability induced by nearby cells [23] [Fig. 1(c)]. Both flow-induced cell reorientation processes were captured by the cell-based model [Figs. 1(b) and 1(c)].

In the second growth phase (Fig. 2), cells in the outer shell of the biofilm are still exposed to the flow, whereas the core of the biofilm is sheltered by surrounding cells and extracellular matrix. We found that the location within the biofilm determines which cell alignment dynamics dominates: cells that are exposed to the flow at the upstream end of the biofilm continue to be realigned vertically owing to the torques τ_{drag} and τ_{shear} [Figs. 2(a) and 2(b)], whereas cells elsewhere in the outer shell of the biofilm continue to align with the flow, mainly owing to τ_{drag}, maintaining asymmetric growth of the biofilm overall. In particular, growth of the horizontally aligned cells in the downstream region causes distinctive dropletlike shapes, which is captured by continuum simulations of growing biofilms with cell alignment fields consisting of a downstream region of flow-aligned cells [Figs. 2(a)–2(c)]. However, cells in the core of the biofilm are not exposed to the flow, so their dynamics are dominated by growth; these cells are subject to a previously observed growth-induced buckling instability [23,40–42] and the "inverse domino" effect of being surrounded by already vertical cells [23]. We thus conclude that the combination of the flow- and growth-induced realignment processes leads to a gradient in the vertical alignment of cells from the upstream end to the downstream end of the biofilm and a wave of cellular verticalization that travels through the biofilm from upstream to downstream [Fig. 2(e)].

In the third growth phase (Fig. 3), the majority of cells in the biofilm are sheltered from the flow, and growth dominates the cell alignment dynamics. Owing to the growth-induced buckling instability and verticalization wave, we observed that biofilms contain a core of highly vertically aligned cells [Fig. 3(a)]. Sheltered cells in the center of the biofilm have a similar dynamics to those in biofilms in low-flow environments, where the shear is not strong enough to reorient cells [17,19,23].

We used the continuum model, which accounts explicitly for directed cell growth, to investigate how the observed cell alignment fields across the phases determine biofilm growth and shape. We found that, in the earlier stages of development, when cells tend to be aligned in a gradient from vertical in the upstream region to horizontal in the downstream region, growth is predominantly in the downstream direction [Fig. 3(b) and Fig. S8 [27]]. As the region of vertical cells expands downstream, growth becomes more symmetric, eventually resembling the symmetric radial expansion of biofilms in weak flow [Fig. 3(b)]. In the final phase, growth is preferentially upward owing to the predominance of vertical cells (Fig. S8). The agreement between the growth dynamics observed in our experiments and continuum simulations (Fig. S9) suggests that the competition between flow-aligned and vertical growth is sufficient to explain biofilm growth in flow for biofilms with up to several thousand cells.

In the past, deformation and shear-induced erosion have been hypothesized to explain the flow-induced symmetry breaking of bacterial biofilms in flow [16,19]. Although this is expected to be true for the extremely large shear rates experienced in turbulent flow, or for bacterial species
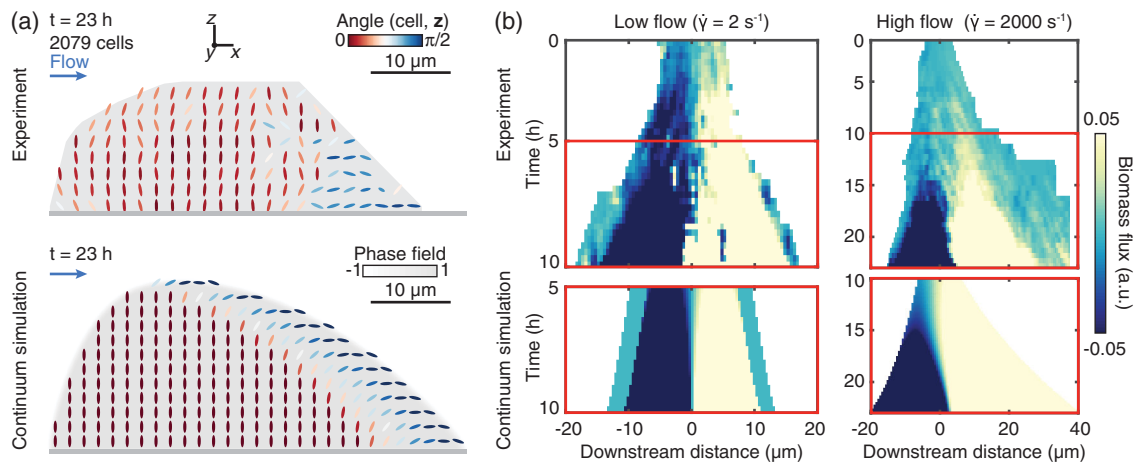

FIG. 3. Biofilms transition from asymmetric to symmetric growth in the final phase of their development in flow. (a) In the final phase of growth, most of the cells in the biofilm are vertical, with only a small region of flow-aligned cells on the downstream side. The gray area denotes the region inside the convex hull around grid points with a cell number density higher than 0.1 μm^{-3} per biofilm ($n = 3$). (b) Growth-induced cumulative biomass flux through the yz plane at each downstream distance; positive and negative values correspond to flux in the downstream and upstream direction, respectively. In low flow, growth is always symmetric (left). In high flow (right), growth symmetry is broken in the early phases, but as more cells verticalize, the biofilm transitions to symmetric growth, which is also captured by continuum simulations (bottom). In experiments (top, $n = 3$), biomass flux measurements were obtained using optical flow [17]. In continuum simulations (bottom), the solution for the flow field inside the biofilm was used to calculate cumulative biomass flux.

with weak matrix, we discovered that the asymmetric growth of cells reoriented by the flow is sufficient to account for the architectures of biofilms in our experiments ($\dot{\gamma} = 2000$ s^{-1}). In this physiologically relevant flow regime, shear-induced erosion has been shown to be resisted by the increased production of cell-cell adhesion proteins [17]. Although some cells are still carried away by the flow [Fig. 1(c)], the effect of erosion is negligible for the architecture dynamics. We now show that deformation is also negligible for biofilms in our experiments. The fluid, which has the viscosity of water μ_w, exerts a stress on the biofilm of approximate magnitude $\mu_w \dot{\gamma}$ so that, by matching stresses at the fluid-biofilm interface, the strain needed to balance the external stress is approximately $\epsilon = \mu_w \dot{\gamma}/G \sim 10^{-3}$, since biofilms have hydrogel-like material properties with elastic modulus $G \sim 10^3$ Pa [43]. Therefore a *V. cholerae* biofilm will not be significantly deformed by the flow, and over growth time-scales, a balance between the internal elasticity and external flow appears instantaneous, with growth then occurring along nematic directions. This supports the hypothesis that nematically aligned growth is the key determinant of bacterial biofilm shape.

The above experimental and numerical results show that flow initially breaks the symmetry in the cell alignment field of growing biofilms. Because cells grow in the direction of their longest axis, the altered cell orientations significantly affect biofilm architecture, causing distinctive dropletlike shapes. In later stages, cells verticalize in a wave that travels from the upstream end to the downstream end of the biofilm, which eventually causes a transition from asymmetric flow-aligned growth to symmetric growth of the biofilm colony, even in the presence of strong flow. In contrast with previous assumptions, deformation and shear-induced erosion are not important determinants of biofilm architecture for the shear rates studied here. Individual cell dynamics are crucial for understanding the architecture of growing biofilms and must be tracked carefully when characterizing the effect of external fields on biofilm growth.

---

*k.drescher@mpi-marburg.mpg.de
†dunkel@mit.edu

[1] L. Hall-Stoodley, J. W. Costerton, and P. Stoodley, Nat. Rev. Microbiol. **2**, 95 (2004).

[2] T. Liu, Y. F. Cheng, M. Sharma, and G. Voordouw, J. Pet. Sci. Eng. **156**, 451 (2017).

[3] D. R. Simpson, Water Res. **42**, 2839 (2008).

[4] K. Werdan, S. Dietz, B. Löffler, S. Niemann, H. Bushnaq, R.-E. Silber, G. Peters, and U. Mueller-Werdan, Nat. Rev. Cardiol. **11**, 35 (2014).

[5] C. M. Dejea, P. Fathi, J. M. Craig, A. Boleij, R. Taddese, A. L. Geis, X. Wu, C. E. D. Shields, E. M. Hechenbleikner, D. L. Huso *et al.*, Science **359**, 592 (2018).

[6] P. E. Kolenbrander, Annu. Rev. Microbiol. **54**, 413 (2000).

[7] S. Lecuyer, R. Rusconi, Y. Shen, A. Forsyth, H. Vlamakis, R. Kolter, and H. A. Stone, Biophys. J. **100**, 341 (2011); A. S. Utada, R. R. Bennett, J. C. Fong, M. L. Gibiansky, F. H. Yildiz, R. Golestanian, and G. C. Wong, Nat. Commun. **5**, 4913 (2014); G. A. O'Toole and G. C. Wong, Curr. Opin. Microbiol. **30**, 139 (2016).

[8] P. S. Stewart, Biofouling **28**, 187 (2012).

[9] M. K. Kim, F. Ingremeau, A. Zhao, B. L. Bassler, and H. A. Stone, Nat. Microbiol. **1**, 15005 (2016).

[10] P. K. Singh, S. Bartalomej, R. Hartmann, H. Jeckel, L. Vidakovic, C. D. Nadell, and K. Drescher, Curr. Biol. **27**, 3359 (2017).

[11] Y. Yawata, J. Nguyen, R. Stocker, and R. Rusconi, J. Bacteriol. **198**, 2589 (2016).

[12] M. C. Marchetti, J. F. Joanny, S. Ramaswamy, T. B. Liverpool, J. Prost, M. Rao, and R. A. Simha, Rev. Mod. Phys. **85**, 1143 (2013).

[13] A. Doostmohammadi, J. Ignés-Mullol, J. M. Yeomans, and F. Sagués, Nat. Commun. **9**, 3246 (2018).

[14] R. J. Allen and B. Waclaw, Rep. Prog. Phys. **82**, 016601 (2019).

[15] A. Welker, T. Cronenberg, R. Zöllner, C. Meel, K. Siewering, N. Bender, M. Hennes, E. R. Oldewurtel, and B. Maier, Phys. Rev. Lett. **121**, 118102 (2018).

[16] B. Purevdorj, J. W. Costerton, and P. Stoodley, Appl. Environ. Microbiol. **68**, 4457 (2002).

[17] R. Hartmann, P. K. Singh, P. Pearce, R. Mok, B. Song, F. Díaz-Pascual, J. Dunkel, and K. Drescher, Nat. Phys. **15**, 251 (2019).

[18] I. Hug, S. Deshpande, K. S. Sprecher, T. Pfohl, and U. Jenal, Science **358**, 531 (2017).

[19] K. Drescher, Y. Shen, B. L. Bassler, and H. A. Stone, Proc. Natl. Acad. Sci. U.S.A. **110**, 4345 (2013).

[20] M. Klotz, M. Kretschmer, A. Goetz, S. Ezendam, O. Lieleg, and M. Opitz, RSC Adv. **9**, 11521 (2019).

[21] K. Drescher, J. Dunkel, C. D. Nadell, S. van Teeffelen, I. Grnja, N. S. Wingreen, H. A. Stone, and B. L. Bassler, Proc. Natl. Acad. Sci. U.S.A. **113**, E2066 (2016).

[22] J. Yan, A. G. Sharo, H. A. Stone, N. S. Wingreen, and B. L. Bassler, Proc. Natl. Acad. Sci. U.S.A. **113**, E5337 (2016).

[23] F. Beroz, J. Yan, Y. Meir, B. Sabass, H. A. Stone, B. L. Bassler, and N. S. Wingreen, Nat. Phys. **14**, 954 (2018).

[24] S. Samijo, J. Willigers, R. Barkhuysen, P. Kitslaar, R. Reneman, P. Brands, and A. Hoeks, Cardiovasc. Res. **39**, 515 (1998).

[25] A. Campesi, M. O. Cerri, C. O. Hokka, and A. C. Badino, Bioproc. Biosyst. Eng. **32**, 241 (2009).

[26] H. C. Fu, T. R. Powers, and R. Stocker, Proc. Natl. Acad. Sci. U.S.A. **109**, 4780 (2012).

[27] See Supplemental Material at http://link.aps.org/supplemental/10.1103/PhysRevLett.123.258101 for further details of the individual cell-based model, the continuum model and the experimental system.

[28] P.-G. De Gennes and J. Prost, *The Physics Of Liquid Crystals*, International Series of Monographs on Physics (Oxford University Press, Oxford, 1995).

[29] F. Chang and K. C. Huang, BMC Biol. **12**, 54 (2014).

[30] Z. You, D. J. G. Pearce, A. Sengupta, and L. Giomi, Phys. Rev. X **8**, 031065 (2018).

[31] D. Dell'Arciprete, M. Blow, A. Brown, F. Farrell, J. S. Lintuvuori, A. McVey, D. Marenduzzo, and W. C. Poon, Nat. Commun. **9**, 4190 (2018).

[32] K. J. Burns, G. M. Vasil, J. S. Oishi, D. Lecoanet, and B. P. Brown, arXiv:1905.10388.

[33] T. Zhang, N. G. Cogan, and Q. Wang, SIAM J. Appl. Math. **69**, 641 (2008).

[34] S. Srinivasan, N. C. Kaplan, and L. Mahadevan, eLife **8**, e42697 (2019).

[35] J. Happel and H. Brenner, *Low Reynolds Number Hydrodynamics: With Special Applications to Particulate Media* (Kluwer, Dordrecht, 1983).

[36] G. B. Jeffery, Proc. R. Soc. A **102**, 161 (1922).

[37] D. Saintillan and M. J. Shelley, *Complex Fluids in Biological Systems* (Springer, New York, 2015), pp. 319–355, https://link.springer.com/chapter/10.1007%2F978-1-4939-2065-5_9.

[38] B. J. Cooley, S. Dellos-Nolan, N. Dhamani, R. Todd, W. Waller, D. Wozniak, and V. D. Gordon, New J. Phys. **18**, 045019 (2016).

[39] M.-C. Duvernoy, T. Mora, M. Ardré, V. Croquette, D. Bensimon, C. Quilliet, J.-M. Ghigo, M. Balland, C. Beloin, S. Lecuyer, and N. Desprat, Nat. Commun. **9**, 1120 (2018).

[40] M. Asally, M. Kittisopikul, P. Rué, Y. Du, Z. Hu, T. Çağatay, A. B. Robinson, H. Lu, J. Garcia-Ojalvo, and G. M. Süel, Proc. Natl. Acad. Sci. U.S.A. **109**, 18891 (2012).

[41] M. A. Grant, B. Wacław, R. J. Allen, and P. Cicuta, J. R. Soc. Interface **11**, 20140400 (2014).

[42] Z. You, D. J. Pearce, A. Sengupta, and L. Giomi, Phys. Rev. Lett. **123**, 178001 (2019)

[43] J. Yan, A. Moreau, S. Khodaparast, A. Perazzo, J. Feng, C. Fei, S. Mao, S. Mukherjee, A. Košmrlj, N. S. Wingreen, B. L. Bassler, and H. A. Stone, Adv. Mater. **30**, 1804153 (2018).

Supplemental Material:
Flow-induced symmetry breaking in growing bacterial biofilms

Philip Pearce,[1] Boya Song,[1] Dominic J. Skinner,[1] Rachel Mok,[1,2] Raimo Hartmann,[3]
Praveen K. Singh,[3] Hannah Jeckel,[3] Jeffrey S. Oishi,[1,4] Knut Drescher,[3,5] and Jörn Dunkel[1]

[1] *Department of Mathematics, Massachusetts Institute of Technology, Cambridge MA 02139-4307, USA*
[2] *Department of Mechanical Engineering, Massachusetts Institute of Technology, Cambridge, MA 02139-4307, USA*
[3] *Max Planck Institute for Terrestrial Microbiology, Marburg, Germany*
[4] *Department of Physics, Bates College, Lewiston, ME 04240, USA*
[5] *Department of Physics, Philipps-Universität Marburg, Marburg, Germany*
(Dated: October 24, 2019)

SINGLE CELL AGENT-BASED SIMULATIONS

Model description

Our single cell model is based on the agent-based framework described in [1], with modifications to include the effect of the flow on the cells and cell-cell polar adhesion. Cells are modeled as ellipsoids of half-length l and half-width r; each cell is described by its position $\boldsymbol{x}$, orientation $\hat{\boldsymbol{n}}$ and effective local viscosity μ . The dynamics of the cells are approximated as over-damped, as cells live at low Reynolds number $Re \approx 10^{-4}$ [1]. Denoting the identity matrix by $\boldsymbol{I}$ and the dynamic viscosity of water by μ_w, the over-damped translational and orientational dynamics for a single cell are

$$
\begin{aligned}
\frac{\mathrm{d}\boldsymbol{x}}{\mathrm{d}t} &= \boldsymbol{\Gamma}^{-1}\left(-\frac{\partial U_{bdy}}{\partial \boldsymbol{x}} - \frac{\partial V}{\partial \boldsymbol{x}} - \frac{\partial U_s}{\partial \boldsymbol{x}}\right) + \frac{\mu_w}{\mu}\boldsymbol{v}_{flow} \\
\frac{\mathrm{d}\hat{\boldsymbol{n}}}{\mathrm{d}t} &= \left(\boldsymbol{I} - \hat{\boldsymbol{n}}\hat{\boldsymbol{n}}^T\right)\left[\boldsymbol{\Omega}^{-1}\left(-\frac{\partial U_{bdy}}{\partial \hat{\boldsymbol{n}}} - \frac{\partial V}{\partial \hat{\boldsymbol{n}}} - \frac{\partial U_s}{\partial \hat{\boldsymbol{n}}}\right)\right] + \frac{\mu_w}{\mu}\boldsymbol{\omega}_{flow}
\end{aligned}
\tag{1}
$$

where $\boldsymbol{\Gamma}$, $\boldsymbol{\Omega}$ are

$$
\begin{aligned}
\boldsymbol{\Gamma} &= \gamma_m\left[\gamma_\parallel\left(\hat{\boldsymbol{n}}\hat{\boldsymbol{n}}^T\right) + \gamma_\perp\left(\boldsymbol{I} - \hat{\boldsymbol{n}}\hat{\boldsymbol{n}}^T\right)\right] \\
\boldsymbol{\Omega} &= \omega_m\omega_R\boldsymbol{I}.
\end{aligned}
$$

Here, γ_m and ω_m are the typical translational and rotational drag coefficients for Stokes drag in the extracellular matrix for a spheroid ($\gamma_m = 6\pi\mu r$, $\omega_m = 8\pi\mu l r^2$) [1]. $\gamma_\parallel$, $\gamma_\perp$ and ω_R are dimensionless geometric parameters characterizing the longitudinal and transverse friction parameters that depend only on the aspect ratio $a = l/r$ of the cell [1].

The pairwise cell-cell interactions are described by two potentials V and U_s, where V is the general pairwise cell-cell interaction that applies to all pairs of cells [1], and U_s is the polar attachment that only exists between two sibling cells after division. For two cells α and β, let l_α and l_β be their half-lengths, r_α and r_β be their widths, $\hat{\boldsymbol{n}}_\alpha$ and $\hat{\boldsymbol{n}}_\beta$ be their orientation vectors, $r_{\alpha\beta}$ be the distance between their centroids, and $\hat{\boldsymbol{r}}_{\alpha\beta}$ be the unit vector pointing from the centroid of cell α to the centroid of cell β. The general pairwise cell-cell interaction potential between these two cells, which accounts for short-range cell-cell repulsion due to steric forces, cell-cell repulsion due to osmotic pressure, and cell-cell attraction mediated by adhesion molecules such as RbmA, follows the cell-cell interaction potential formula in [1]

$$
U_{\alpha\beta} = \epsilon_0\epsilon_1\left[\nu_{steric}\exp\left(-\frac{\rho_{\alpha\beta}^2}{\lambda_{r,\,steric}^2}\right) + \exp\left(-\frac{\rho_{\alpha\beta}^2}{\lambda_r^2}\right) + \frac{\nu}{1 + \exp\left(\frac{\rho_a - \rho_{\alpha\beta}}{\lambda_a}\right)}\right].
$$

Here $\rho = \frac{r_{\alpha\beta}}{\sigma}$ is the cell-cell distance normalized by the overlap shape factor $\sigma(l_\alpha, l_\beta, r_\alpha, r_\beta, \hat{\boldsymbol{n}}_\alpha, \hat{\boldsymbol{n}}_\beta, \hat{\boldsymbol{r}}_{\alpha\beta})$ in [1]. The strength of $U_{\alpha\beta}$ is described by ϵ_0 and adjusted by the shape factor $\epsilon_1(l_\alpha, l_\beta, r_\alpha, r_\beta, \hat{\boldsymbol{n}}_\alpha, \hat{\boldsymbol{n}}_\beta)$,

depending on the relative cell orientations and cell shapes. ν_{steric} describes the relative strength of the steric cell-cell repulsion, $\lambda_{r,\,steric}$ describes the range of the steric cell-cell repulsion, λ_r describes the range of the osmotic cell-cell repulsion, ν describes the relative strength of cell-cell attraction, ρ_a describes the attraction position, and λ_a describes the width of the cell-cell attraction. The cell-cell potential also has an associated translational relaxation time τ_t, which can be interpreted as a time scale of how long it takes for a bacterium to reach an equilibrium configuration from the cell-cell interaction potential. We used the same values as in [1] for the model parameters $\lambda_{r,\,steric}$, λ_r, ν, ρ_a and λ_a. The value of ϵ_0 was increased compared with [1], in order to account for the increase of the cell-flow interaction energy ϵ_{flow} in the simulations with increased flow; therefore τ_t was slightly decreased. We found that choices of $\epsilon_0 = 10^4 \epsilon_{flow}$, $\nu_{steric} = 1$ and $\tau_t = 5.65$ s were sufficient to ensure the cells do not overlap in these simulations; the osmotic and the short-range steric parts of the repulsion were both necessary for this. All the interaction potential parameter values are listed in Table II. For a single cell α in a biofilm with N cells, V is the total potential for all $N-1$ pairwise cell-cell interactions between cell α and other $N-1$ cells β ($V = \sum_{\beta=1,\beta\neq\alpha}^{N} U_{\alpha\beta}$).

We model the polar cell-cell attachment after division using a harmonic spring between two sibling cells with spring constant k_s and natural length r_s. As soon as a cell divides, a spring is assigned between the two closest endpoints of the daughter cells, with the spring potential

$$U_s = k_s \left(r_{endpoint} - r_s \right)^2,$$

where $r_{endpoint}$ is the distance between the two closest endpoints. To match with experiments, where polar cell-cell adhesion was observed to last for approximately one division time, the spring breaks at $0.9 \cdot \tau_g$ after division, where τ_g is the average doubling time measured from single-cell experimental data using the same technique as [1]. The natural spring length r_s was chosen to match the cell half-width for simplicity. The spring constant k_s was chosen to be large enough such that cells are not carried away by the flow immediately after division in the initial stages of biofilm growth. The values of ϵ_s, r_s, k_s and τ_g are listed in Table II.

The interaction between cells and the wall boundary is modeled with the same repulsive interaction potential as in [1]

$$U_{bdy} = \begin{cases} 0 & z_o \leq 0 \\ \epsilon_{bdy} \exp\left(\frac{z_o}{\sigma_{bdy}}\right) & z_o > 0 \end{cases}$$

where ϵ_{bdy} captures the magnitude of the cell-boundary interaction, and σ_{bdy} captures the range of the interaction. z_o is an overlap coordinate defined as $z_o = l|\hat{\boldsymbol{n}} \cdot \hat{\boldsymbol{N}}| + r - \hat{\boldsymbol{N}} \cdot (\boldsymbol{x} - \boldsymbol{S})$ where $\hat{N}$ is the normal vector of the plane, and $\boldsymbol{S}$ is any point on the plane. Here we use $\hat{N} = [0,0,1]$ and $\boldsymbol{S} = [0,0,0]$ such that the wall is the xy-plane that crosses the origin. The values of $\epsilon_r = \epsilon_{bdy}/\epsilon_0$ and σ_{bdy}, listed in Table II, were chosen to be the same as the values in [1].

The instantaneous cell length growth follows the growth equation in [1]

$$\frac{\mathrm{d}l}{\mathrm{d}t} = \frac{l}{\tau_g} \ln(2) \tag{2}$$

where l is the instantaneous half-length of the cell and τ_g is the average doubling time. Cell widths are constant throughout simulations. A cell divides when it grows an additional length Δl from its birth length, where Δl is drawn from a Gaussian distribution with mean l_{add} and standard division σ_{add}. Cells divide into two daughter cells that have half the length of their parent cells and the same orientation as their parent cell. The values of l_{add} and l_{add} were fitted according to the experimental distribution of cell lengths. Both values are listed in Table II.

To account for the increase in the local effective viscosity of a cell as extracellular polymeric substances (EPS) matrix and cell-cell adhesion proteins are produced by itself and the surrounding cells, we used two steps to calculate the local viscosity μ experienced by each cell. First, to account for extracellular matrix and adhesion protein generation by each cell, the individual local viscosity contribution of a cell is a sigmoid function that increases from μ_w to μ_{max}, where μ_w is the viscosity of water. Let t_{age} be the cell's age, scaled

2

by the cell's division time. The individual local viscosity contribution of the cell is

$$\mu_{indv} = \mu_{max} - \frac{\mu_{max} - \mu_w}{1 + \exp\left(\frac{t_{age} - t_0}{\Delta t}\right)}$$

where $t_0 = 0.4$ is the viscosity transitional time and $\Delta t = 0.1$ is the viscosity-increase time scale (both are a proportion of the cell's age). The left panel of Figure S1 shows a plot of of μ_{indv} as a function of t_{age}. Then, to account for extracellular matrix and adhesion proteins generated by neighboring cells, the local viscosity experienced by a cell α is taken to be the Gaussian-filtered value of the individual local viscosity contributions of the surrounding cells

$$\mu_\alpha = \sum_{\beta=1}^{N} \frac{1}{\sqrt{\pi}\sigma_{vis}} \exp\left(-\frac{r_{\alpha\beta}^2}{\sigma_{vis}^2}\right) \mu_{indv,\,\beta},$$

where σ_{vis} is the viscosity averaged length scale and $r_{\alpha\beta}$ is the distance between the centroids of cell α and cell β. The right panel of Figure S1 shows the local viscosity distribution of a simulated biofilm with 250 cells. The viscosity parameters $\mu_{max} = 2 \cdot 10^5$ Pas and $\sigma_{vis} = 1.39$ µm were chosen by matching the translational and rotational dynamics of cells aligning with the flow in simulated biofilms with those of experimental ones (Fig. S2). The value of μ_{max} is listed in Table II.
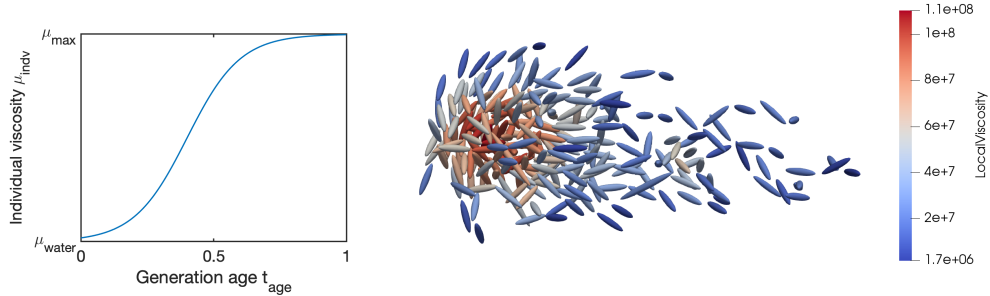

FIG. S1. Left: μ_{indv} as a function of cell generation age t_{age}. Right: The top view of a simulated biofilm with 250 cells, where cells are colored by their local viscosity.

When the biofilm is equal to or smaller than 20 cells, we approximate the flow field as the linear shear flow $\boldsymbol{v}_{flow} = \dot{\gamma}z\hat{\boldsymbol{x}}$, where z is the height of the cell above the surface and $\dot{\gamma}$ is the constant shear rate of the linear shear flow. When the biofilm is larger than 20 cells, we approximate the flow field around the biofilm by a linear shear flow passing over a hemispherical bump on a plane floor. The center of the hemispherical bump is located at the xy-center of the biofilm, and the radius of the hemispherical bump is approximated as the 25th percentile of distances between all the cells to the xy-center of the biofilm. Let a be the radius of the hemispherical bump, and (x_c, y_c, z_c) be the position of the center of the hemispherical bump in Cartesian coordinates. For a point (x, y, z) in Cartesian coordinates, define spherical polar coordinates (r, θ, ϕ) by

$$\frac{x - x_c}{a} = r\sin\theta\cos\phi, \ \frac{y - y_c}{a} = r\sin\theta\sin\phi, \ \frac{z - z_c}{a} = r\cos\theta$$

so that the boundary of the hemisphere is given by $r = 1, \theta \in [0, \pi/2]$, and the planar floor is given by
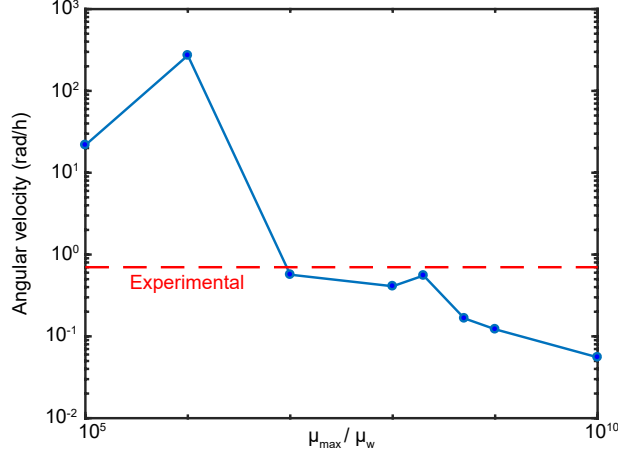
FIG. S2. Average angular velocity of simulated cells aligning to the flow direction from their orientation at birth as a function of maximum viscosity μ_{max}/μ_w, where μ_w is the viscosity of water. The value $\mu_{max} = 2 \cdot 10^8 \mu_w$ was chosen to recreate the average angular velocity of flow-aligning cells measured in experiments (0.7 rad/h, dashed red line), while ensuring cells are not carried away by the flow.

$r \geq 1, \theta = \pi/2$. From [2], the flow velocity $\boldsymbol{v}_{flow}$ at (x, y, z) is

$$\frac{\boldsymbol{v}_{flow}}{\dot{\gamma}} = z\hat{\boldsymbol{x}} - \left(u \cos\phi \hat{\boldsymbol{r}} + v \cos\phi \hat{\boldsymbol{\theta}} + w \sin\phi \hat{\boldsymbol{\phi}} \right)$$
$$= \left[z - (u \sin\theta + v \cos\theta) \cos^2\phi + w \sin^2\phi \right] \hat{\boldsymbol{x}}$$
$$- (u \sin\theta + v \cos\theta + w) \cos\phi \sin\phi \hat{\boldsymbol{y}}$$
$$+ (-u \cos\theta \cos\phi + v \sin\theta \cos\phi) \hat{\boldsymbol{z}}$$

where u, v, w are functions of r and θ:

$$u(r, \theta) = \cos\theta W(r, \cos\theta) + \frac{1}{2} \sin\theta \left[U(r, \cos\theta) + V(r, \cos\theta) \right]$$
$$v(r, \theta) = -\sin\theta W(r, \cos\theta) + \frac{1}{2} \cos\theta \left[U(r, \cos\theta) + V(r, \cos\theta) \right]$$
$$w(r, \theta) = \frac{U(r, \cos\theta) - V(r, \cos\theta)}{2}.$$

U, V and W are functions of r and $\cos\theta$. Let P_m^n denote an associated Legendre function in $\cos\theta$ of degree n and order m. The expressions of U, V and W from [2] are:

$$W(r, \cos\theta) = \frac{1}{2} \sum_{n=1}^{\infty} \frac{1}{r^{2n+1}} \left[A_{2n+1} \left(\cos\theta P_{2n+1}^1 + \frac{P_{2n}^1}{2n} \right) + r A_{2n} \cos\theta P_{2n}^1 \right]$$
$$U(r, \cos\theta) = \frac{1}{2} \sum_{n=1}^{\infty} \frac{P_{2n+1}^2}{r^{2n+1}} \left(\frac{A_{2n+1} \cos\theta}{2n} + \frac{r A_{2n}}{4n+1} \right)$$
$$+ \frac{1}{2} \sum_{n=2}^{\infty} \frac{P_{2n-1}^2}{(n-1)(2n-1)r^{2n}} \left[\frac{(2n-3)(2n+1)A_{2n}}{4n+1} + G_{2n} \right] \tag{3}$$
$$V(r, \cos\theta) = -\frac{1}{2} \sum_{n=1}^{\infty} \frac{(2n+1)P_{2n+1}^0}{r^{2n+1}} \left(A_{2n+1} \cos\theta + \frac{2nr A_{2n}}{4n+1} \right) + \sum_{n=1}^{\infty} \frac{G_{2n} P_{2n-1}^0}{r^{2n}}.$$

We followed [2] to take the first fifteen terms in Eqs. (3) with the coefficients recorded in Table I.

4

n	A_{2n+1}	A_{2n}	G_{2n}
1	-2.04530	2.75543	1.65326
2	-0.86783	1.82574	-0.73104
3	0.14321	0.08434	-0.06369
4	-0.04430	-0.04420	0.05474
5	0.01643	0.02520	-0.04337
6	-0.00640	-0.01535	0.03381
7	0.00232	0.00985	-0.02643
8	-0.00054	-0.00659	0.02083
9	-0.00024	0.00455	-0.01657
10	0.00057	-0.00323	0.01331
11	-0.00069	0.00235	-0.01079
12	0.00070	-0.00174	0.00881
13	-0.00067	0.00131	-0.00725
14	0.00062	-0.00100	0.00601
15	-0.00056	0.00077	-0.00500

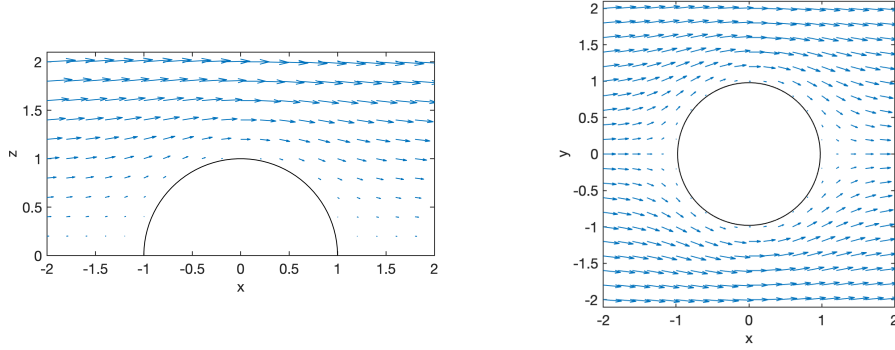TABLE I. First fifteen of $\{A_{2n+1}, A_{2n}, G_{2n}\}$ in Eqs. (3) [2].

FIG. S3. $\boldsymbol{v}_{flow}/\dot{\gamma}$ for $y = 0$ on the xz-plane (left) and for $z = 0.2$ on the xy-plane (right).

Let $a = l/r$ be the aspect ratio of a bacterium. The rotation caused by the shear flow is computed according to [3]

$$\boldsymbol{\omega}_{flow} = (\boldsymbol{I} - \hat{\boldsymbol{n}}\hat{\boldsymbol{n}}^T) \left[\frac{a^2 - 1}{a^2 + 1} \frac{\nabla \boldsymbol{v}_{flow} + \nabla \boldsymbol{v}_{flow}^T}{2} + \frac{\nabla \boldsymbol{v}_{flow} - \nabla \boldsymbol{v}_{flow}^T}{2} \right] \hat{\boldsymbol{n}}.$$

The flow velocity gradient $\nabla \boldsymbol{v}_{flow}$ is computed using a central difference scheme with $\Delta x = \Delta y = \Delta z = 0.01r$.

The key parameters used for the simulations are shown in Table II.

Parameter	Value	Unit	Description
r	0.2775	µm	Average half-width of the bacteria [1].
τ_g	8630	s	Growth time constant (average cell division time of biofilm-associated cells in strong flow, $\dot{\gamma} = 2000\ \mathrm{s}^{-1}$, obtained from experiments).
$\dot{\gamma}$	2000	s^{-1}	Experimental shear rate.
μ_w	1	mPa·s	Dynamic viscosity of water at room temperature.
μ_{max}	$2 \cdot 10^5$	Pa·s	Estimate of the maximal effective dynamic viscosity, owing to extracellular matrix and adhesion proteins, at room temperature.
ϵ_r	10		Ratio comparing the strength of bacteria-boundary interaction to the strength of the bacteria-bacteria interaction ($\epsilon_r = \epsilon_{bdy}/\epsilon_0$) [1].
σ_{bdy}	0.2775	µm	Non-dimensional boundary potential length scale parameter [1].
τ_t	5.65	s	Translational time scale due to repulsion in matrix (typical time needed for daughter cells in matrix to reach their equilibrium configurations due to repulsion after cell division).
l_{add}	1.01	µm	Average value of length added to bacteria after division to compute division length.
σ_{add}	0.08	µm	Standard deviation of length added to bacteria after division to compute division length.
ϵ_0	$5 \cdot 10^{-14}$	J	Strength of the osmotic pressure-mediated cell-cell repulsion.
ν_{steric}	1		Relative strength of the steric cell-cell repulsion.
$\lambda_{r,\,steric}$	0.83		Range of the steric cell-cell repulsion (corresponds to 0.58 µm at a typical overlap factor of $\sigma = 0.7$µm, which is the value it would take for a sphere with the typical mean cell volume of 0.4µm³) [1].
λ_r	1.65		Range of the osmotic pressure-mediated cell-cell repulsion (corresponds to 1.16 µm at a typical overlap factor of $\sigma = 0.7$µm) [1].
ν	0.13		Relative strength of the attractive part of the cell-cell potential [1].
λ_a	0.16		Well-width of the attractive part of the cell-cell potential [1].
ρ_a	2.93		Position of the attractive part of the cell-cell potential [1].
k_s	$6.5 \cdot 10^{-1}$	J·µm^{-2}	Spring constant for the additional directional cell-cell attraction.
r_s	0.2775	µm	Natural length of the spring between sibling cells.

TABLE II. Simulation parameters.

Model implementation

A custom, highly parallelized individual cell-based code employing graphics processing units (GPUs) was developed to perform the simulations based on [1]. At each time step, cell-cell interactions between all pairs of cells are evaluated. A standard explicit Euler scheme is used to numerically integrate Eqs. (1) and Eq. (2) in non-dimensional form, with $r = 0.2775$µm as the length scale [1], the translational time $\tau_t = 5.65$s as the time scale [1] and $\epsilon = 5 \cdot 10^{-20}$J [1] as the energy scale.
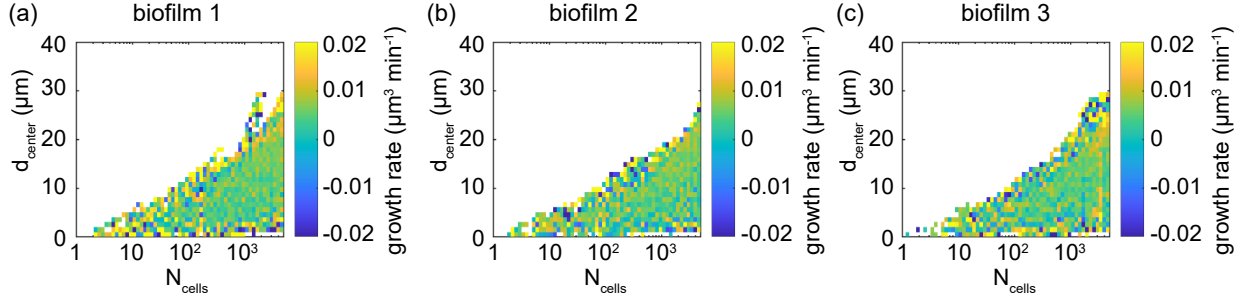
FIG. S4. Heatmaps showing spatially resolved single-cell measurements of growth rate inside three different biofilms (a)-(c) at $\dot{\gamma} = 2000\text{s}^{-1}$ [1]. The growth rate is spatially uniform throughout development.

CONTINUUM SIMULATIONS

Model description

A biofilm is a mixture of several phases, including cells, extracellular polymeric substances (EPS) and adhesion proteins. In addition to mechanical phases, there are also other relevant fields such as a nematic order field describing cell orientations and nutrient concentration fields. Multi-phase continuum equations for growing biofilms have been postulated [4], which can describe inhomogeneous biofilms with spatial nutrient gradients. However, during the early stages of biofilm growth, the nutrient concentration is approximately constant, as is the growth rate (Fig. S4) [1]. We assume that when the continuum model is applicable, the relative volume fraction of cells and extracellular matrix stays approximately constant, and that the nutrients needed for growth diffuse into the biofilm in a way that does not effect the mechanics. These assumptions are only valid during the early stages of growth, but allow us to treat the biofilm mechanically as a single phase system. The specific form of the mechanics is then determined by the constitutive relation for the stress tensor $\boldsymbol{\sigma}$. We take the system as growing, but otherwise incompressible, i.e. the biofilm grows but the density does not significantly fluctuate, an assumption that is valid only in the early stages of biofilm development. In this case, we must solve a modified incompressibility condition

$$\nabla \cdot \boldsymbol{v} = g.$$

Neglecting inertia, the momentum balance takes the form,

$$\nabla \cdot \boldsymbol{\sigma}^{dev} = \nabla p,$$

where $\boldsymbol{\sigma}^{dev}$ is the deviatoric part of the stress tensor. All that remains is to choose a constitutive law for $\boldsymbol{\sigma}^{dev}$ which accounts for both passive and growth stresses. A full constitutive model would account for the viscoelastic matrix component as well as the nemato-elasticity conferred by the nematic ordering of the cells. For the minimal continuum model we seek a simplified constitutive law that describes the long time growth of the biofilm along nematic directions

The extracellular matrix is known to behave viscoelastically, [4] however, a viscoelastic liquid behaves as a viscous fluid over time scales longer than the relaxation time scale. Since growth occurs over relatively long time scales, we assume that the extracellular matrix simply contributes a viscous part to the constitutive equation.

Biofilms are living liquid crystals and have an internal nematic order [1, 5]. We introduce a nematic order parameter $\boldsymbol{Q}$ measuring the local alignment of the cells [6, 7]. Aside from growth, there are two contributions to the constitutive relation. First, there is a free energy associated with the alignment of the cells; thus any distortion away from an aligned state has an energetic cost, and causes a stress to be exerted on the material. Second, there is anisotropic dissipation depending on whether the macroscopic flow

7

is aligned with the nematic director or not, and dissipation when the director field rotates relative to the fluid.

To create a minimal continuum model, we neglect any anisotropy in the passive part of the stress tensor, reducing the constitutive equation to that of a Newtonian fluid, $\boldsymbol{\sigma}_p = 2\mu\boldsymbol{D}$, where $\boldsymbol{D} = \frac{1}{2}(\nabla\boldsymbol{v} + \nabla\boldsymbol{v}^T)$. We neglect the external fluid shear stress experienced by the biofilm in order to examine the mechanism of growth along nematic directions together with local flow-induced realignment of cells. Order of magnitude estimates (see main text) show that the external shear is insufficient to account for any noticible change in the shape, so we take the external fluid as initially at rest, and of a low relative viscosity ($\mu_{ext} = 0.1\mu$). We also assume that g is not a function of the pressure or the local alignment strength; each cell grows and divides at a constant rate independent of the nematic ordering, in agreement with experimental measurements (Fig. S4).

To account for growth in our consitutive law, we consider the additional stress caused by directed growth. A growing cell with orientation $\boldsymbol{n}$, and position $\boldsymbol{y}$, exerts a force dipole on the surrounding medium,

$$\boldsymbol{f}(\boldsymbol{x};\boldsymbol{y},\boldsymbol{n}) = f\delta(\boldsymbol{y} + \ell\boldsymbol{n} - \boldsymbol{x})\boldsymbol{n} - f\delta(\boldsymbol{y} - \boldsymbol{x})\boldsymbol{n} \approx -f\ell\boldsymbol{nn} \cdot \nabla_x\delta(\boldsymbol{x} - \boldsymbol{y})$$

To find the additional contribution to the stress tensor due to such dipoles, we use Kirkwood's formula [8],

$$\boldsymbol{\sigma}_g = -f\ell\rho\langle\boldsymbol{nn}\rangle = -\zeta g\langle\boldsymbol{nn}\rangle = -\zeta g\left(\boldsymbol{Q} + \frac{1}{d}\boldsymbol{1}\right).$$

where $\boldsymbol{Q} = \langle\boldsymbol{nn}\rangle - \boldsymbol{1}/d$ is the nematic order parameter, $\zeta > 0$ is a constant, d is the dimension (all simulations were performed with $d = 3$), and we have assumed the strength of the dipole is proportional to the growth rate. The isotropic part of this stress can be absorbed into the pressure; note, however, that the pressure is a Lagrange multiplier for $\nabla \cdot \boldsymbol{v} = g$ and still accounts for growth.

Since $\zeta g = f\ell\rho$ is written in terms of microscopic quantities, its value could in theory be measured. Here, we take a phenomenological approach. Consider a 3D element of biofilm that is surrounded by a zero viscosity fluid at zero pressure. Aligning the nematic axis with $\hat{z}$, we have

$$\boldsymbol{v} = \left(\frac{g - a}{2}x, \frac{g - a}{2}y, az\right),$$

for some $0 < a \leq g$. The combined stress tensor $\boldsymbol{\sigma}^{dev} = \boldsymbol{\sigma}_p^{dev} + \boldsymbol{\sigma}_a^{dev} = -\zeta g\boldsymbol{Q} + 2\mu\boldsymbol{D}$ is diagonal, with

$$\sigma_{xx}^{dev} = \sigma_{yy}^{dev} = \mu(g - a) + \zeta gS/3$$
$$\sigma_{zz}^{dev} = 2\mu a - 2\zeta gS/3,$$

where $Q_{xx} = Q_{yy} = -S/3$, $Q_{zz} = 2S/3$, and S is the strength of alignment. We suppose that for $S = 1$, i.e. perfect alignment in the $\hat{z}$ direction, the only motion is in the $\hat{z}$ direction. This is possible only for $\zeta = 2\mu$. A similar calculation in 2-dimensions requires $\zeta = \mu$, so

$$\zeta = (d - 1)\mu.$$

The full continuum equations inside the growing biofilm can be written as

$$\nabla \cdot \boldsymbol{v} = g$$
$$\nabla \cdot \boldsymbol{\sigma}^{dev} = \nabla p$$
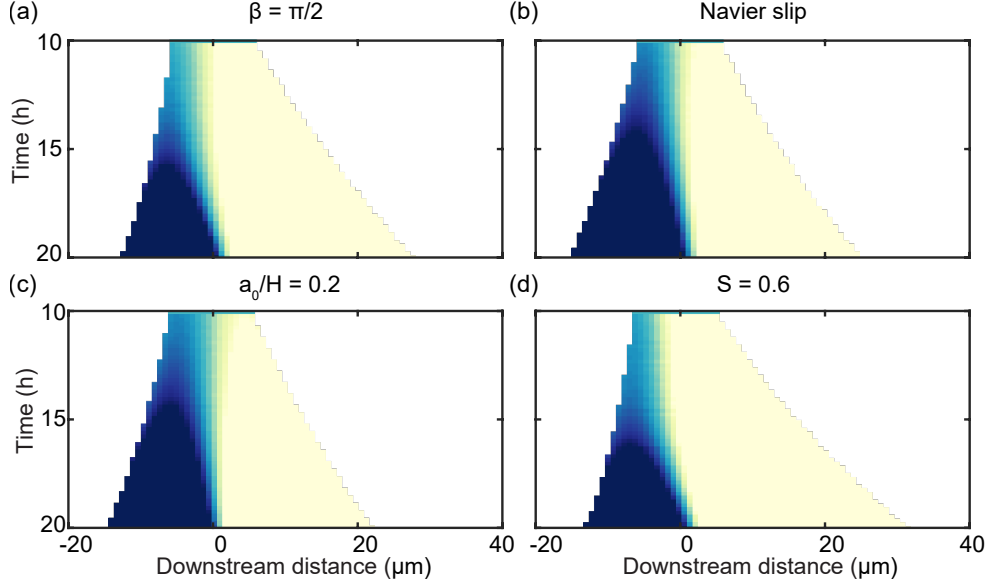$$\boldsymbol{\sigma}^{dev} = 2\mu\boldsymbol{D} - (d - 1)\mu g\boldsymbol{Q}.$$

8

FIG. S5. The continuum model's prediction of a transition from asymmetric to symmetric growth is not sensitive on the model parameters, and is recreated robustly for (a) downstream angle $\beta = \pi/2$, (b) a standard Navier slip condition, (c) director field transition length at the back of the biofilm $a_0/H = 0.2$ and (d) nematic order parameter $S = 0.6$. The values of these parameters used in the main paper are summarized in Table III.

Boundary conditions

This minimal continuum model represents growth along an imposed nematic direction. In order to simulate the model, we must impose boundary conditions at the biofilm-fluid, and biofilm-surface interface. We take the external fluid as initially at rest, at which point the phase-field method automatically enforces continuity at the internal interface.

At the biofilm-surface interface we impose a modified Navier-slip condition, which can be written as

$$\mu \frac{\partial u}{\partial z} = e_s(1 - (\boldsymbol{n} \times \hat{z})^2)u,$$

$$\mu \frac{\partial v}{\partial z} = e_s(1 - (\boldsymbol{n} \times \hat{z})^2)v,$$

$$w = 0,$$

where $\boldsymbol{v} = (u, v, w)$, we have assumed the surface is defined by $z = 0$, and e_s is a slip parameter. The modification from a regular Navier-slip is the inclusion of the $(1 - (\boldsymbol{n} \times \hat{z})^2)$, where $\boldsymbol{n}$ is the nematic director. This is to reflect the fact that horizontal cells continue to grow, leading to biofilm movement along the surface in areas with many horizontal cells, whereas vertical cells are fully attached to the surface, resisting movement along the surface. We found that simulations with a regular Navier-slip condition did not produce qualitatively different results (Fig. S5).

Imposed nematic field

In our minimal continuum model, we do not directly solve for the nematic field, but impose it based on experimental data (see Fig. 2e in the main text). Physically, the director field is set by interactions between the cells and the flow, the cells and the wall, and cell-cell interactions. Verticalization of cells at the base of
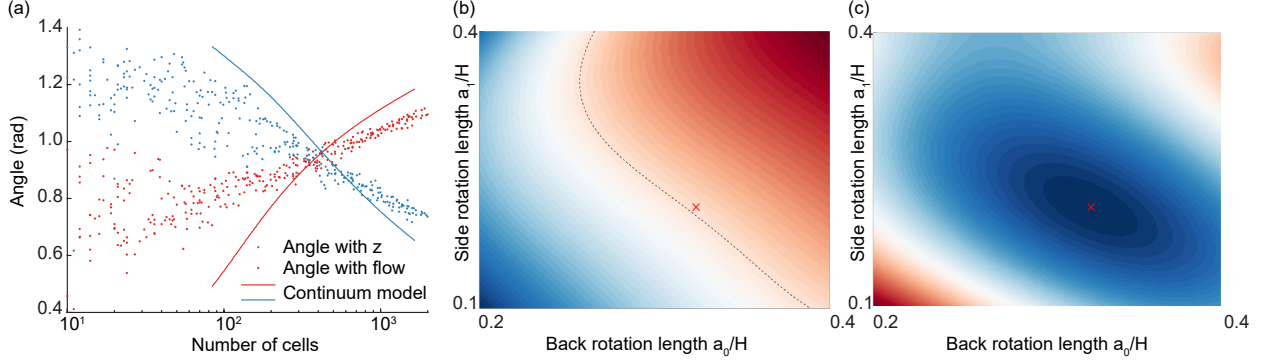
FIG. S6. Key governing parameters in the continuum model and quantitative justification for their values. (a) Average angle with z (blue) or the flow direction (red) versus number of cells for experiments (dots) and continuum simulations with chosen values of the key parameters a_0 and a_1 (lines). The time variable in continuum simulations was converted to number of cells by fitting an exponential curve to time versus number of cells for $n = 3$ biofilms and rearranging the obtained equation. (b) Dependence of the time of transition between phases 2 and 3, as defined in Fig. 1a, on the parameters a_0 and a_1 in the continuum model. The line shows the values for which the transition time is 17h, which is approximately the value found in experiments. Note that a transition still occurs for a range of values of a_0 and a_1, showing that the choice of their values does not qualitatively affect the results (see also Fig. S5). (c) Mean-squared distance (MSD) between average angle curves shown in (a) and experimental values. The values of a_0 and a_1 were taken to be the values that minimized the MSD. The heatmaps in (b) and (c) were generated by performing 24 simulations and interpolating between them. The red crosses in (b) and (c) show the chosen values of a_0 and a_1.

the biofilm quickly propagates into the interior, with only a boundary layer of cells at the edge rotated by the flow. We seek a minimal continuum model to investigate how growth along nematic directions affects the shape of the biofilm without being a full mechanical model accounting for all stresses and strains of the system. Therefore we impose the nematic order based on experimental measurements, acknowledging that this is set by interactions at the single cell scale that our minimal continuum model does not account for.

We take the nematic director as $\boldsymbol{n} = (n_x, n_y, n_z) = (\cos\alpha_0, \sin\alpha_0 \sin\alpha_1, \sin\alpha_0 \cos\alpha_1)$. The angle α_0 is calculated based on the relative distance to the back of the biofilm; given a point (x, y, z) within the biofilm, the back defined as (x^*, y, z), with $x^* = \max_s\{s|(s, y, z) \text{ is in biofilm}\}$. The angle α_0 changes linearly over a distance a_0 from the back, so that

$$\alpha_0 = \min\left\{\frac{\pi}{2} - \beta\frac{x - x^* - a_0}{a_0}, \ \frac{\pi}{2}\right\} \tag{4}$$

where β is the angle through which the director field is rotated. A value of $\beta = 1.25 \cdot \frac{\pi}{2}$ was used in simulations, so the director rotates from being vertical at the front of the biofilm, to being slightly beyond horizontal at the back, as observed in experiments (see Fig. 3 in the main paper). The rotation through α_1 ensures that the director rotates outwards, away from the central plane of the biofilm, defined by $y = y_c$.

The angle α_1 is defined similarly to α_0, but calculated based on the distance to either the left or the right side of the biofilm. Defining $y_+ (y_-) = \max_s (\min_s)\{s|(x, s, z) \text{ is in biofilm}\}$, we take

$$\alpha_+ = \max\left\{\frac{\pi}{2}\frac{(y - y_+ + a_1)}{a_1}, 0\right\}, \qquad \alpha_- = \min\left\{-\frac{\pi}{2}\frac{(y - y_- + a_1)}{a_1}, 0\right\},$$

$$\alpha_1 = \alpha_+ + \alpha_-.$$

We found that the numerical results did not depend qualitatively on the parameters a_0, a_1, or β; a transition from asymmetric to symmetric growth occured for a wide range of values of these parameters (Fig. S5). However, the choices of a_0 and a_1 were the key quantitative control parameters in the model that determined when the transition occured (Fig. S6).

10

Numerical phase-field method

To solve for the biofilm growth numerically we use the phase-field method for complex fluids [9]. We introduce an order parameter ϕ, where $\phi = +1$ in the biofilm and $\phi = -1$ outside. When $\phi = \pm 1$ the equations become the governing equations of each phase. The only regions where this is not true are the interfacial regions. The width of the interfacial region is set by the choice of mixing energy, which penalizes interfaces whilst encouraging demixing. By reducing the size of the interface one can take a limit of the phase-field equations to formally recover the sharp interface equations with correct surface boundary conditions. Thus, by solving the phase field equations, with a small interface region, one can approximately solve the full problem without needing to explicitly keep track of the internal interfaces.

Our equations only differ from [9], in that in our formulation $\nabla \cdot \boldsymbol{v} \neq 0$, and consequently an additional term $g(1 - \phi^2)/2$ appears in the Cahn-Hilliard equation, representing growth in interfacial regions. The phase field equations are,

$$\nabla \cdot \boldsymbol{v} = \frac{1 + \phi}{2} g,$$

$$0 = -\nabla p + \nabla \cdot \boldsymbol{T},$$

$$\boldsymbol{T} = \frac{1 + \phi}{2} \boldsymbol{\sigma}_b^{dev} + \frac{1 - \phi}{2} \boldsymbol{\sigma}_w - \lambda \nabla \phi \otimes \nabla \phi,$$

$$\phi_t + \boldsymbol{v} \cdot \nabla \phi = \frac{g(1 - \phi^2)}{2} + \gamma_1 \lambda \nabla^2 \left[-\nabla^2 \phi + \frac{\phi(\phi^2 - 1)}{\epsilon^2} \right],$$

$$\boldsymbol{\sigma}_{ext} = 2\mu_{ext} \boldsymbol{D},$$

$$\boldsymbol{\sigma}_b^{dev} = 2\mu \boldsymbol{D} - (d - 1)\mu g \boldsymbol{Q},$$

where ϵ controls the width of the interface, λ controls the strength of surface tension and is set so the effective capillary number is large. A large capillary number ensures that the system is not dominated by surface tension, so that the biofilm can take non-hemispherical shapes; here it is important to reiterate that deformation by the imposed flow is not a key driving process of the biofilm dynamics (as discussed in the main text), and is therefore not accounted for in our continuum model. A large capillary number also means that the contact angle condition does not affect the numerical solution. γ_1 sets the time scale for phase field diffusion, and μ_w is the viscosity of water. All parameters used are listed in Table III. Boundary conditions on ϕ are given by

$$\boldsymbol{m} \cdot \nabla \phi = 0,$$

$$\boldsymbol{m} \cdot \nabla \nabla^2 \phi = 0,$$

for a boundary with normal $\boldsymbol{m}$, which, when combined, represent no flux and a contact angle of 90° [9].

We solve the equations in a channel of height H, width H, and length $4H$. As long as H is large enough to contain the biofilm, the choice of H does not affect the solution. We non-dimensionalize the equations using H as a length scale, $1/g$ as a time scale (so that $\boldsymbol{v} = Hg\boldsymbol{v}^*$, where $\boldsymbol{v}^*$ is dimensionless) and similar for
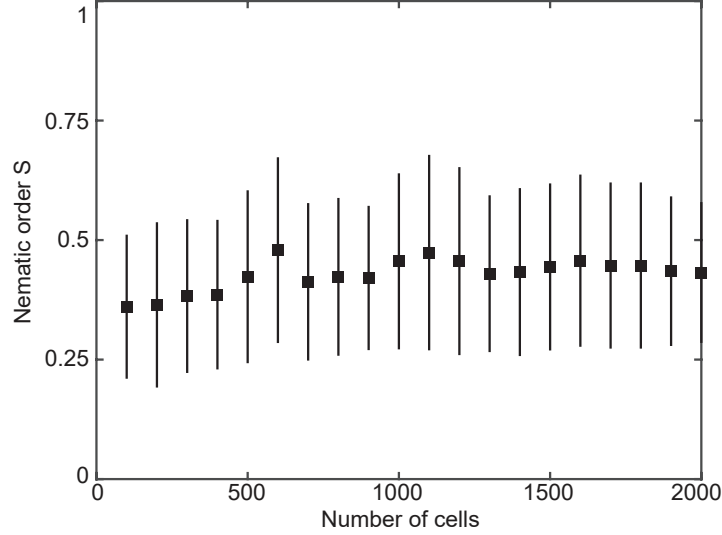
FIG. S7. Mean nematic order parameter S at gridpoints spaced 2 μm throughout $n = 3$ biofilms. Error bars show the standard deviation.

other variables. The equations become

$$
\begin{aligned}
\nabla^* \cdot \boldsymbol{v}^* &= \frac{1+\phi}{2} g^*, \\
0 &= -\nabla^* p^* + \nabla^* \cdot \boldsymbol{T}^*, \\
\boldsymbol{T}^* &= \frac{1+\phi}{2} \boldsymbol{\sigma}_b^* + \frac{1-\phi}{2} \boldsymbol{\sigma}_w^* - \frac{\lambda}{g\mu H^2} \nabla^*\phi \otimes \nabla^*\phi, \\
\phi_{t^*}^* + \boldsymbol{v}^* \cdot \nabla^*\phi &= \frac{g(1-\phi^2)}{2} + \frac{\gamma_1 \lambda}{gH^4} \nabla^{*2}\left[-\nabla^{*2}\phi + \frac{\phi(\phi^2-1)}{(\epsilon/H)^2}\right], \\
\boldsymbol{\sigma}_{ext}^* &= 2\frac{\mu_{ext}}{\mu} \boldsymbol{D}^*, \\
\boldsymbol{\sigma}_b^* &= 2\boldsymbol{D}^* - (d-1)\boldsymbol{Q},
\end{aligned}
\tag{5}
$$

where we can identify a number of dimensionless groups. By relating the parameter λ, to an effective surface tension, $\sigma_{eff} = \frac{2\sqrt{2}}{3}\lambda/\epsilon$, we can rewrite some of the dimensionless groups in terms of a Capillary number, $Ca = \mu Hg/\sigma_{eff}$. The resulting dimensionless groups and dimensional parameters are summarized in Table III.

At the start of the continuum simulations, the biofilm is a spherical cap with radius r_0 and origin $(0, 0, z_0)$. We took $z_0 < 0$, so that the initial shape was flatter than a hemisphere, to slightly better match the biofilm shape in experiments without breaking the initial symmetry in the xy-plane, although this did not affect the results strongly. The initial dimensional radius of the biofilm was assumed to be approximately 6 μm, in agreement with experimental measurements of biofilms at 10 h (see Fig. 3b in the main paper).

We solve the continuum equations (5) using the Dedalus Project [10]. Dedalus is a highly parallelized framework for solving partial differential equations. It uses pseudospectral methods for spatial discretization. We use Chebyshev polynomials in the wall-normal direction to enforce boundary conditions and Fourier polynomials in the streamwise and spanwise direction. The equations are integrated forwards in time using an implicit-explicit Runga-Kutta scheme. All models are run with resolution 384x196^2 in the streamwise, spanwise, and wall-normal directions.

Parameter	Value	Unit	Description
H	40	µm	Height of the channel.
g	1/8630	s^{-1}	Growth rate measured from experiments. For a volume V, a biofilm obeys $\dot{V} = gV$.
Ca	100		Effective capillary number.
ϵ/H	0.01		Ratio of interface thickness and height of the channel.
μ_{ext}/μ	0.1		Ratio of biofilm and external viscosity.
$\gamma_1\mu/H^2$	10^{-4}		Effective diffusivity of the phase-field.
r_0/H	0.17		Ratio of radius of initial spherical cap and height of the channel.
z_0/H	-0.04		Ratio of the origin of initial spherical cap and height of the channel.
β	$1.25 \cdot \frac{\pi}{2}$		Angle through which the director field rotates in the x-z plane.
a_0/H	0.325		Length of region over which the director field rotates at the back of the biofilm.
a_1/H	0.21		Length of region over which the director field rotates at the sides of the biofilm.
e_sH/μ	0.5		Dimensionless slip parameter.
S	0.4		Strength of nematic order measured from experiments (see Fig. S7).

TABLE III. Continuum simulation parameters.

EXPERIMENTAL DETAILS

Experiments were performed using *V. cholerae* strain KDV613, also referred to as WT*, which is a derivative of the N16961 wild type strain (O1 El Tor). Although *V. cholerae* typically displays a slightly curved cell body, the strain KDV613 displays a straight cell shape, owing to the deletion of the *crvA* gene (VCA1075). This strain also carries the low copy number plasmid pNUT542, which harbors the gene coding for the superfolder green fluorescent protein (*sf-gfp*) under the control of a constitutively expressed synthetic promoter (P_{tac}). The constitutive fluorescent signal was used to segment the *V. cholerae* cells in biofilm images as described previously [1]. Further experimental results to complement those in the main paper are shown in Figs. S10 and S11.

Calculations for quantitative definitions of phases

Quantitative definitions of each phase are shown in Fig. 1a. The volume of the shell is the flow-facing surface area of the convex hull multiplied by the cell width. Here the flow-facing surface area is the difference between the total surface area and the surface area of the base (calculated by taking the 2D convex hull in the xy plane). The volume of the core is the remaining volume of the convex hull or zero, whichever is greater. For these calculations, the 10% of cells furthest from the biofilm center of mass were removed to reduce noise and artifacts.
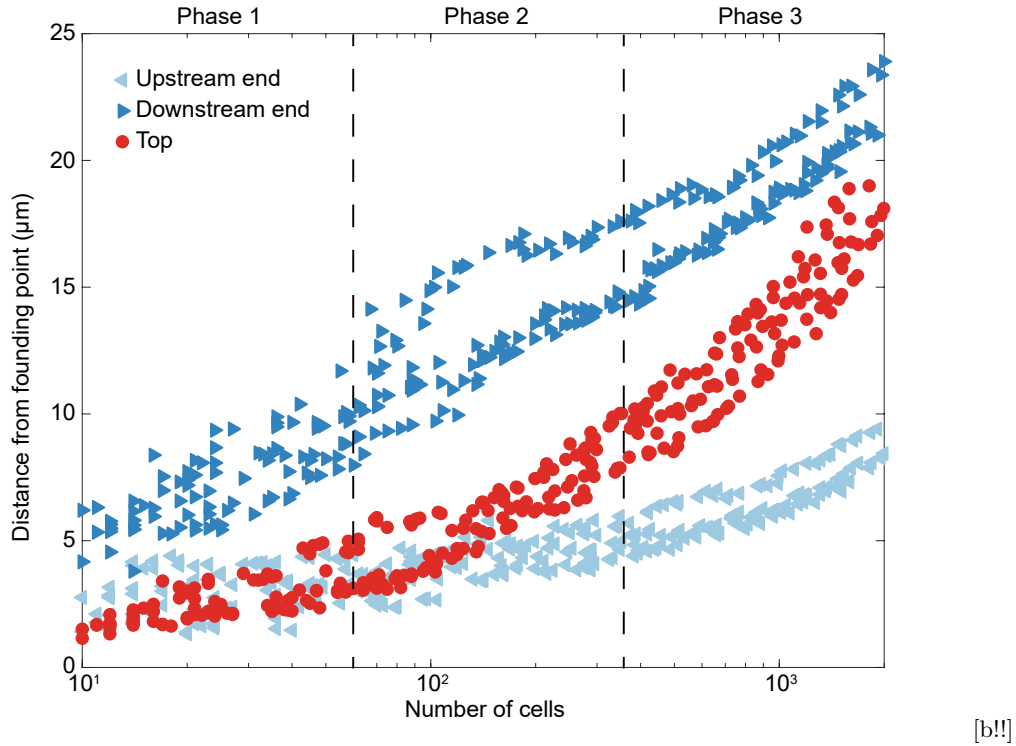
FIG. S8. Expansion characteristics in each growth phase. Each marker shows a distance from the founding point versus number of cells at a single timepoint ($n = 3$ biofilms). The distances were calculated by taking the minimum or maximum cell position in each direction, after removing the 10% of cells furthest from the biofilm center of mass, to reduce noise and artifacts. In phase 1, the biofilm expands fastest downstream. In phase 2, it begins to expand faster vertically, as cells begin to verticalize. In phase 3, most of the cells are vertical and it expands fastest upwards, and roughly equally fast in the upstream and downstream directions.

[1] R. Hartmann, P. K. Singh, P. Pearce, R. Mok, B. Song, F. Díaz-Pascual, J. Dunkel, and K. Drescher, Nat. Phys. **15**, 251 (2019).
[2] T. Price, Q. J. Mech. Appl. Math. **38**, 93 (1985).
[3] G. B. Jeffery, Proc. Royal Soc. A **102**, 161 (1922).
[4] T. Zhang, N. G. Cogan, and Q. Wang, SIAM J. Appl. Math. **69**, 641 (2008).
[5] K. Drescher, J. Dunkel, C. D. Nadell, S. van Teeffelen, I. Grnja, N. S. Wingreen, H. A. Stone, and B. L. Bassler, Proc. Natl. Acad. Sci. U.S.A. **113**, E2066 (2016).
[6] P.-G. De Gennes and J. Prost, *The Physics Of Liquid Crystals (International Series Of Monographs On Physics)* (Oxford University Press, 1995).
[7] A. Doostmohammadi, J. Ignés-Mullol, J. M. Yeomans, and F. Sagués, Nat. Commun. **9**, 3246 (2018).
[8] R. B. Bird, C. F. Curtiss, R. C. Armstrong, and O. Hassager, *Dynamics of polymeric liquids: Kinetic theory* (Wiley, 1987).
[9] P. Yue, J. J. Feng, C. Liu, and J. Shen, J. Fluid Mech. **515**, 293 (2005).
[10] K. J. Burns, G. M. Vasil, J. S. Oishi, D. Lecoanet, and B. P. Brown, arXiv:1905.10388 (2019).
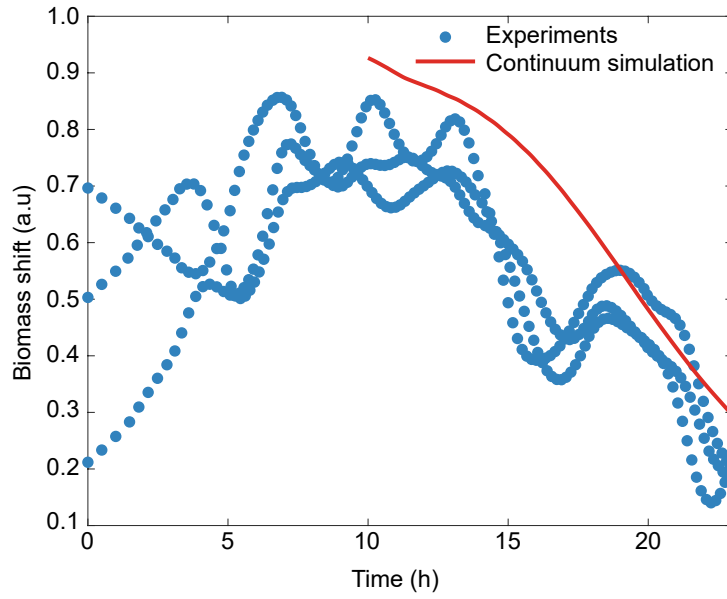
FIG. S9. Biomass shift versus time from experimental measurements ($n = 3$ biofilms) and continuum simulations. Biomass shift is defined as the sum of the biomass flux (shown in Fig. 3b of the main paper) along the flow direction, normalized by the sum of the absolute values, as described in [1].
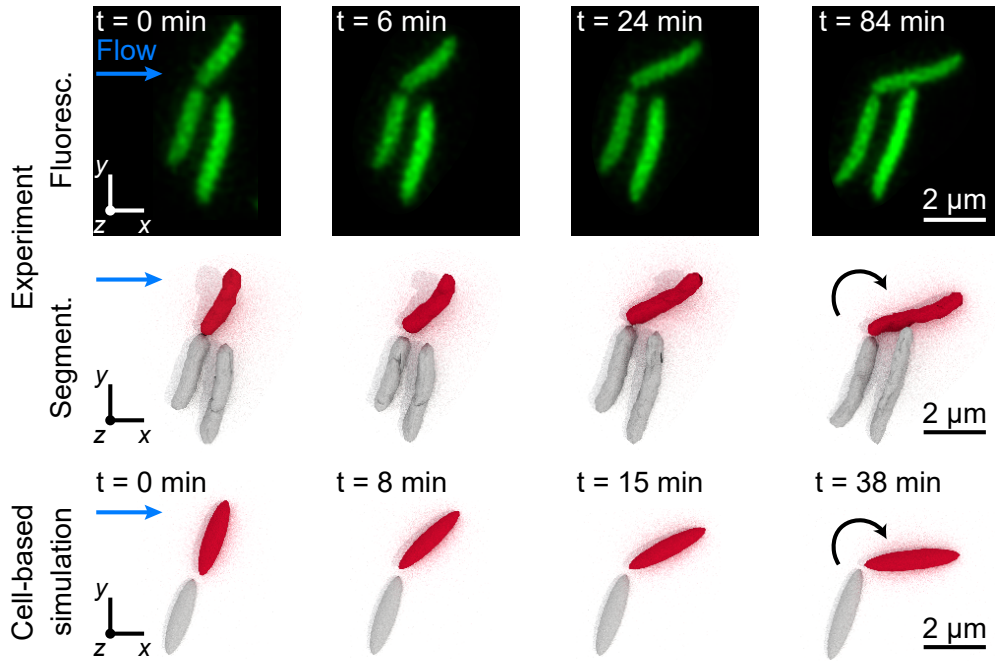

FIG. S10. Intermediate time steps in rotation of cell shown in the Main Text Fig. 1b.
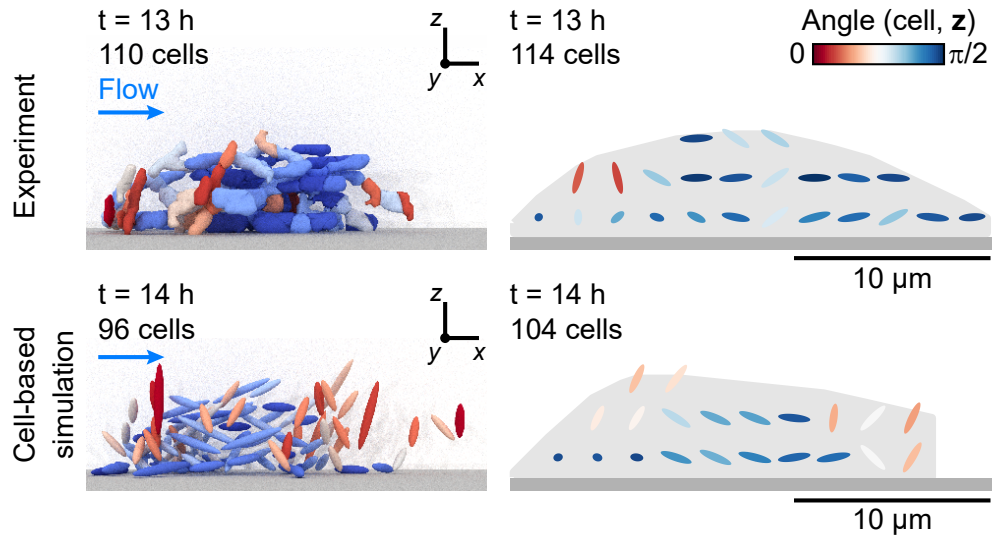
FIG. S11. In the early stages of growth, cells are predominantly aligned with the flow, with some vertical cells on the upstream side of the biofilm. The right-hand panels show averaged nematic alignment fields for several experiments ($n = 3$, top) and simulations ($n = 10$, bottom) along the midplane of the biofilm. In each case, the grey area denotes the region inside the convex hull around gridpoints with a cell number density higher than 0.05 μm^{-3} per biofilm. The cell-based simulations recreated the cell alignment fields, consisting of mainly flow-aligned cells with some vertical cells at the front of the biofilm, suggesting that an applied shear is sufficient to explain their observation in our experiments.